



Particle Detector (PD) Experiment of the Korea Space Environment Monitor (KSEM) Aboard Geostationary Satellite GK2A

J. Seon¹ · K.-S. Chae¹ · G.W. Na¹ · H.-K. Seo¹ · Y.-C. Shin¹ · J. Woo¹ · C.-H. Lee¹ · W.-H. Seol¹ · C.-A. Lee¹ · S. Pak¹ · H. Lee¹ · S.-H. Shin¹ · D.E. Larson² · K. Hatch² · G.K. Parks² · J. Sample³ · M. McCarthy⁴ · C. Tindall⁵ · Y.-J. Jeon⁶ · J.-K. Choi⁶ · J.-Y. Park⁶

Received: 30 October 2019 / Accepted: 12 January 2020 / Published online: 27 January 2020
© Springer Nature B.V. 2020

Abstract The Particle Detector (PD) experiment aboard the geostationary satellite GEO-KOMPSAT-2A (GK2A) measures populations of electrons and positive ions in the Earth's geostationary orbit at a geographic longitude of 128.2°E, inclination of 0° and a mean orbital radius of 6.6 Earth radii (R_E). The PD experiment consists of three sensors with different viewing angles relative to the spacecraft. Each sensor consists of two telescopes that are mechanically configured back-to-back with a field-of-view of 20° × 20° and measures electrons and ions, using silicon detectors equipped with foils and magnets for the separation of ions and electrons. The energy ranges of the sensor for electrons and ions are 100–3800 keV and 148–22500 keV, respectively. A particular emphasis on electron measurement is given by allocating 48 energy bins in the measured energy range, whereas 22 energy bins are allocated for ion measurements. This unprecedented energy resolution of $\Delta E/E$ in the range 5–25% for the electron and ion flux measurements is acquired every three seconds with cyclic polling of each sensor every second to provide an effective temporal resolution of one second. Together with the magnetometer aboard the spacecraft, the PD experiment will provide quantitative observations that will enable improved understanding of the adiabatic and nonadiabatic dynamics of the Earth's magnetosphere for space weather studies at geostationary orbits from the vantage point of a far-east longitude.

Keywords Space weather · Geostationary orbit · Radiation belt · Charged particle detector · Silicon detectors

✉ J. Seon
jhseon@khu.ac.kr

¹ School of Space Research, Kyung Hee University, Yongin, 17104, Republic of Korea

² Space Science Laboratory, University of California, Berkeley, CA 94720, USA

³ Department of Physics, Montana State University, Bozeman, MT 59717, USA

⁴ Department of Earth and Space Science, University of Washington, Seattle, WA 98195, USA

⁵ Lawrence Berkeley Laboratory, Berkeley, CA 94720, USA

⁶ Satrec Initiative Co., 21, 1628, Yuseong-daero, Yuseong-gu, Daejeon, 34054, Republic of Korea

1 Introduction

The advent of modern space technology, including artificial satellites at various altitudes and state-of-the-art instrumentation aboard, has allowed new insights into the complicated interactions of the Earth's atmosphere, ionosphere, and magnetosphere with varying conditions from the Sun, planetary, and extraterrestrial sources. Early spacecraft missions accomplished scientific discovery and understanding of the interactions and responses of the Earth's atmospheric, ionospheric, and magnetospheric regions to the Sun by collecting and examining in-situ and remote-sensing data corresponding to extensive ranges of physical parameters (summaries of these findings and theories are available from textbooks, for example, Kivelson and Russell 1995; Parks 2004; Gurnett and Bhattacharjee 2005). Subsequent exploration of the discovered regions beyond the scope of scientific investigation has been performed in the context of conducting activities and operations in various fields such as Earth observation, communication, and space science by sending mostly spacecraft, but also occasionally human beings. These various scientific and social interests, together with broad engineering disciplines associated with the activities, constitute the scope of space weather (Hastings and Garrett 2004; Bothmer and Daglis 2007 and references therein).

In particular, the geostationary orbit has been of great interest as it provides unique opportunities in space in the fields of meteorology, communication, and military because its orbital period matches that of the Earth's rotation, which places the launched spacecraft over a fixed location relative to the ground. Findings from previous space missions indicate that geostationary orbits are usually immersed in the outer radiation belts that are occupied with highly energetic, relativistic electrons (Arnoldy and Chan 1969; Lezniak and Winckler 1970; Bogott and Mozer 1973; Belian et al. 1978; Baker et al. 1982). However, depending on the interplanetary conditions from the Sun, the orbits are also exposed to the plasmasphere of dense and cold charged particles (Lennartsson and Reasoner 1978) or supersonic flow of solar wind outside the Earth's magnetopause (Opp 1968; Cummings and Jr 1968; Skillman and Sugiura 1971). The presence of intense, energetic electrons and the extreme variability of the harsh environment in the geostationary orbits necessitate *in-situ* monitoring of charged particles and magnetic fields to protect priceless human assets, while simultaneously inspiring scientific curiosity with respect to this dynamic region of the Earth's magnetosphere.

The Korea Space Environment Monitor (KSEM) is a suite of instruments that measure fluxes of charged particles and vector magnetic fields at geostationary orbits over the Korean peninsula. KSEM consists of three Particle Detectors (PDs), a Charging Monitor (CM) and a set of two fluxgate sensors on a deployable boom, together with two anisotropic magnetoresistive sensors located within the spacecraft. A dedicated Instrument Data Processing Unit (IDPU) is allocated for the three PDs and CM to handle scientific data, telemetry and spacecraft command, whereas another independent Data Processing Unit handles data, telemetry and commands for the four magnetic sensors comprising the Service Oriented Space Magnetometer (SOSMAG). In Fig. 1 the functional composition of the KSEM instrument is illustrated. In this paper, the instrument design, data analysis, calibration and early flight data from the PDs are presented. Descriptions of SOSMAG and CM are provided in separate papers. Detailed descriptions of instrument configuration and design are provided in Sect. 2, numerical simulation and calibration of the instrument in Sect. 3, followed by flight operation and data in Sect. 4. Section 5 provides a summary and the conclusions of the present paper.

1.1 Objectives of the Instruments

The KSEM instrument provides continuous monitoring of space weather in the geostationary orbit by measuring the populations of charged particles and geomagnetic fields. Ob-

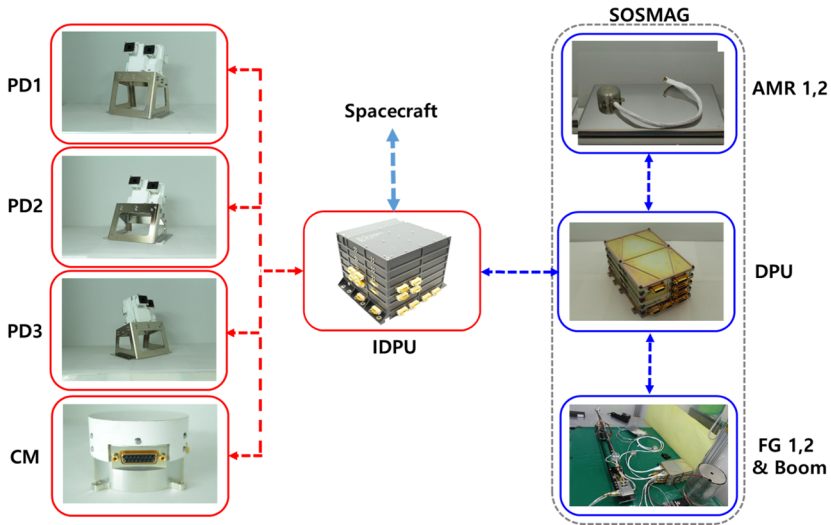


Fig. 1 Configuration of KSEM. KSEM consists of three Particle Detectors (PDs), a Charging Monitor (CM) and a Service Oriented Space Magnetometer (SOSMAG)

Table 1 Particle Detector (PD) instrument specifications

Instrument Parameters	Specification
Energy range	100 keV–3800 keV (Electrons) 148 keV–22500 keV (Protons)
Energy resolution	$0.05 < \Delta E/E < 0.25$
Field-of-view	$20^\circ \times 20^\circ$
FOV directions	6
Geometric factor	$\sim 0.02 \text{ cm}^2 \text{ sr}$ (Attenuator open) $\sim 4 \times 10^{-4} \text{ cm}^2 \text{ sr}$ (Attenuator closed)
Cadence	3 s (cyclic polling of 3 sensors every second)

servations from KSEM at a final longitude of 128.2°E and geocentric distance of $6.6 R_E$ ($R_E = 6378 \text{ km}$, Earth radius) will complement existing geostationary observations at other longitudes, such as those provided by Geostationary Operational Environmental Satellites (GOES). Each of the KSEM user requirements has driven design accommodated in the instrument. The user requirements for the PD were to take measurements of electrons in the energy range of 100 keV to 2 MeV for five (5) different viewing angles with a minimum geometric factor of $10^{-3} \text{ cm}^2 \text{ sr}$. In Table 1, the requirements and specifications of KSEM instruments are summarized. The PD satisfies or exceeds the user requirements for conducting space weather research. There are six (6) viewing angles from three PDs. Each PD consists of two telescopes that are mechanically configured back-to-back with a field-of-view of $20^\circ \times 20^\circ$. The details of the mechanical orientations of the three PDs relative to the spacecraft and the six Fields of View (FOVs) as referenced in geophysical coordinates are provided in Sect. 2.1. Both electrons and ions can be observed by PDs with good energy resolution, which will be essential to quantitative analyses of the outer radiation belt and solar energetic particles. The principle of separating ions and electrons is given in Sect. 2.2.

In consideration of the limited downlink speed from the spacecraft to the ground, the electron and ion flux measurements are acquired every three seconds with a cyclic polling of the three PDs every second.

1.2 Instrument Heritage

The PD sensor in this paper inherits its design from the Solar Energetic Particle (SEP) Investigation on MAVEN (Larson et al. 2015) and the Solid State Telescope (SST) on Time History of Events and Macroscale Interactions during Substorms (THEMIS) missions (Larson and Moreau 2009). Subsequent design modifications have been made to increase the detection energies of electrons according to the requirements described in the previous section. A greater number of thicker detectors and analog signal chains are necessary to increase the measured energy range of electrons and ions. The sensor housing dimensions are accordingly increased to accommodate thicker detector stacks and to provide more shielding to the anticipated penetration of energetic particles in the radiation belt. In addition, a reduction of the Field-of-View (FOV), which in turn yields a reduction of the geometric factor of the instrument, is made in consideration of the expected large number of detector counts in the Earth's outer radiation belts. A detailed description of this design is provided in Sects. 2.2 and 2.3.

2 Instrument Description

The PD instrument consists of three sensors that are identical in design, named PD1, PD2, and PD3, with different viewing angles relative to the spacecraft. Each PD consists of a pair of identical, double-ended solid-state telescopes that are mechanically configured back-to-back. The sensor head of each PD is mounted on a mechanical pedestal to determine its viewing angle relative to the spacecraft. The photos of flight models PD1, PD2, and PD3 in Fig. 1 show the sensor heads assembled with mechanical pedestals that differ in height and tilting angle. Each sensor head consists of two telescopes that are configured back-to-back to measure primarily electrons and ions. The telescopes, named A and B, have Open (O) and Foil (F) sides. The O-side of telescope A (AO) views the same direction as the F-side of telescope B (BF), constituting one of the six (6) FOVs provided by the PD instruments. The mechanical configuration of each sensor head is presented together with naming conventions and physical dimensions of the outer envelope in Fig. 2. The FOV of each PD is determined by its baffled collimators and apertures (shown normal to blue and red arrows in Fig. 2). The FOV of the PD is rectangular in shape, and measures $20^\circ \times 20^\circ$ in angular size.

2.1 Mechanical Configuration Relative to Spacecraft

All the PD sensor heads are mounted on the bottom surface of the spacecraft, as illustrated in Fig. 3. The surface of sensor heads are overlain with gold colored Multi-Layer Insulator (MLI) together with the rest of the spacecraft for thermal control of the spacecraft system. The positions of the three PDs are indicated with red arrows in the figure, together with a definition of spacecraft coordinates. The vertical direction in the figure is parallel to the Z-axis of the spacecraft ($+Z_{sc}$), whereas the stowed boom of the Service Oriented Space MAGnetometer on (Magne et al. 2019) the $+X_{sc}$ surface of the spacecraft, as indicated in the figures, deploys along the $+X$ -axis of the spacecraft. With a nominal attitude of the spacecraft in orbit, the X-, Y- and Z-axes of the spacecraft point along the velocity direction

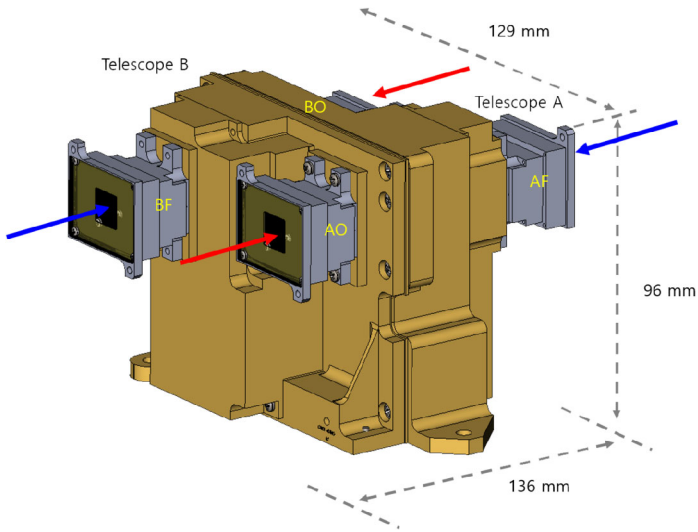
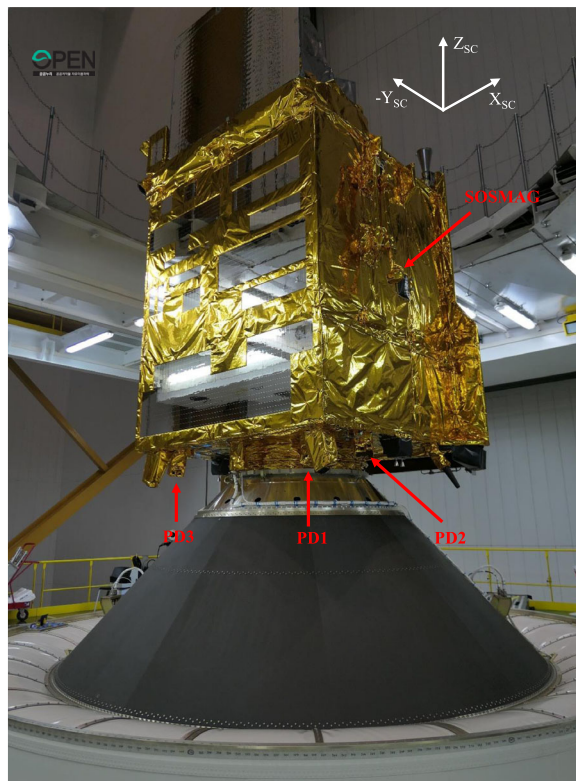


Fig. 2 Configuration, dimensions and naming convention of PD. Each PD consists of a pair of double-ended, back-to-back telescopes intended for measuring electrons and ions separately. The Open side (O) and Foil side (F) of the telescope are indicated for each telescope. The entrance apertures of the telescopes are the square areas normal to the arrows in the figure. The outermost dimension of each PD is also given in the figure

Fig. 3 GK2A spacecraft at launch site. PD1, PD2, and PD3 are mounted on the bottom surface of the spacecraft, viewing different angles in space. Also shown is the definition of the spacecraft coordinate system. This image is provided by the Korean Aerospace Research Institute (KARI) and is publicly available at <https://www.kari.re.kr>



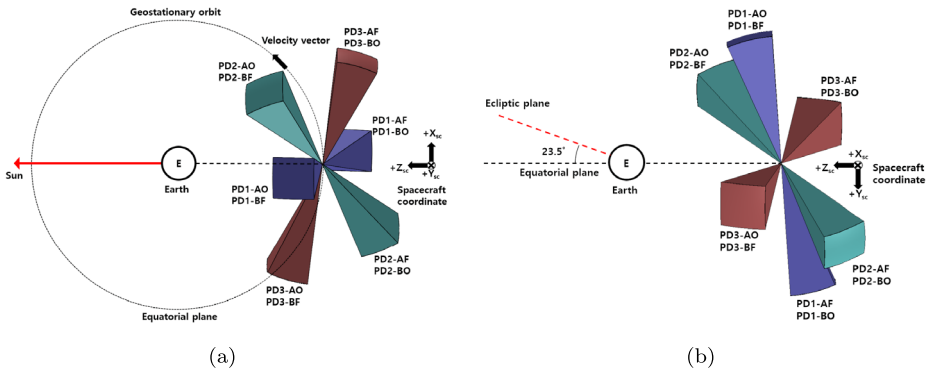


Fig. 4 Illustration of Fields of View (FOVs) for PD1, PD2 and PD3 with respect to the spacecraft coordinate system. With a nominal spacecraft attitude of nadir-pointing along the Z-axis, the X-axis of the spacecraft coordinates points along the velocity direction (east), Y-axis points toward the south and the Z-axis points toward the nadir of the spacecraft. The left-hand side of the figure shows FOVs as viewed from the north, whereas a view in the equatorial plane of the Earth is shown on the right-hand side. Each PD has a FOV of $20^\circ \times 20^\circ$ in angular size

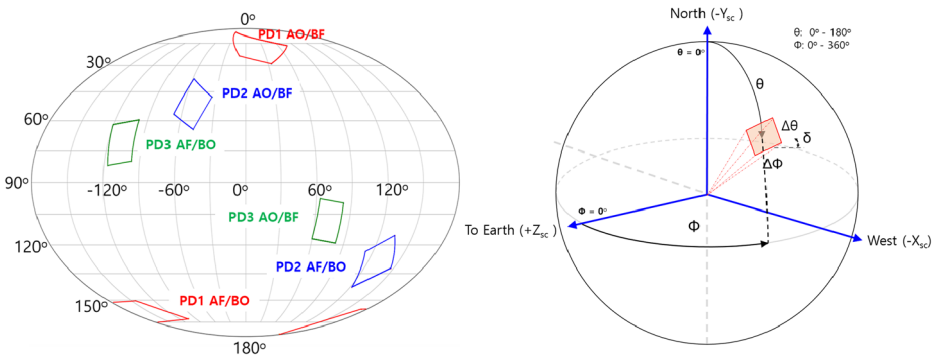


Fig. 5 Fields of View (FOVs) for PD1, PD2 and PD3. The FOV shape of each PD is rectangular with a size of $20^\circ \times 20^\circ$ in angular extent. The FOVs are referenced to the equatorial plane of the Earth according to the nominal attitude of the spacecraft. The Mollweide projection of the FOVs is made in terms of polar and azimuthal angles measured against the north and earthward axes, respectively. Definitions of the polar angle θ and azimuthal angle Φ are given on the right-hand side of the figure

of the spacecraft (east), south, and in the nadir direction, respectively, composing a right-handed coordinate system. The FOVs for each PD, as determined in spacecraft coordinates, are shown in Fig. 4. The FOVs of the PDs are selected to measure the particle fluxes at different pitch angles with respect to the local Earth’s magnetic fields, while avoiding interference from the spacecraft structures or neighboring equipment. The FOV of PD1 is more inclined toward the polar axis (north-south), while the FOV of PD3 is closer to the equatorial plane. In Fig. 5, the Mollweide projection of the FOV for each telescope of the PD is provided with reference to the equatorial plane of the Earth according to the nominal attitude of the spacecraft. The Mollweide projection of the FOVs is made in terms of polar and azimuthal angles measured against the north and earthward axis, respectively. The definitions of the polar angle θ and azimuthal angle Φ are provided on the right-hand side of the figure. The

Table 2 The boresight directions for each PD. The definitions of angular variables θ , φ , δ are also shown in Fig. 5. The boresights of PDs are listed in the increasing order of the colatitude angle θ in the table

Telescope	PD Boresight		
	θ	φ	δ
PD1 AO/BF	15	25	55
PD2 AO/BF	51	308	60
PD3 AF/BO	71	252	7
PD3 AO/BF	109	72	7
PD2 AF/BO	129	128	60
PD1 AF/BO	165	205	55

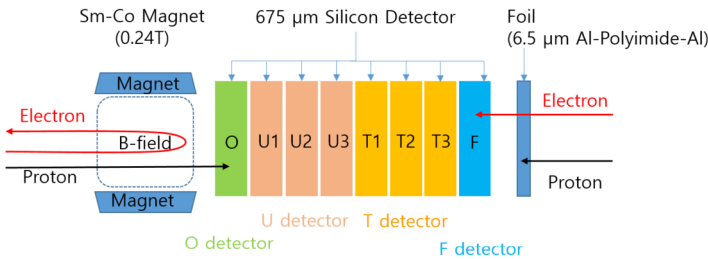


Fig. 6 Schematic representation of the PD detector stack. A single 675- μm -thick silicon detector is placed on the outer sides of the stack for O and F detectors, whereas three detectors of the same thickness are wire-bonded in parallel to construct U and T detectors in the middle. The F-side of the detector is covered with a 6.5- μm foil to stop ions with energies below 350 keV. The O-side detector is placed next to a yoked Sm-Co magnet that produces a magnetic field strength of 0.24 T. The generated magnetic field deflects electrons with energies below 350 keV. Ions are not significantly affected by the magnetic field due to larger gyro-radii

angular positions of the FOV centers (boresight) for each PD as expressed in terms of the angles are listed in Table 2.

2.2 Sensor Configuration

There are four stacks of doped silicon detectors in each telescope of the PD, as shown in Fig. 6. The outer detectors, O and F, are single detectors that are 675 μm thick, while the middle detectors, U and T, consist of three 675- μm -thick detectors that are wire-bonded together in parallel, providing an effective thickness of 2025 μm each. Therefore, a set of eight 675- μm -thick silicon detectors provide the total stopping power with respect to the electrons and ions for each detector stack of the PD telescope. The outer sides of O and U detectors are further covered with 90-nm-thick aluminum to suppress sensitivity of the detectors to low-energy photons. The F-side of the detector stack is covered with a 6.5 μm Al-Polyimide-Al foil to stop ions with energies of <350 keV/nucleon, whereas on the opposite side of the detector stack, the O-side, magnetic fields are generated by yoked Sm-Co magnets. There are four magnets, each with a maximum energy product of 24 MGOe and a coercivity of 9.8 kOe, to produce about 0.24 T of magnetic field strength at the center of the O-side aperture. The magnetic field sweeps away electrons with energies <350 keV. To meet the spacecraft requirements on the residual magnetic moment, the directions of the magnetic fields produced by the magnets are anti-parallel to each other for telescopes A and B.

Each PD unit is equipped with a set of four (4) co-moving mechanical attenuator paddles with small pinholes. The attenuator paddles are rotated into the FOVs of both sides of the

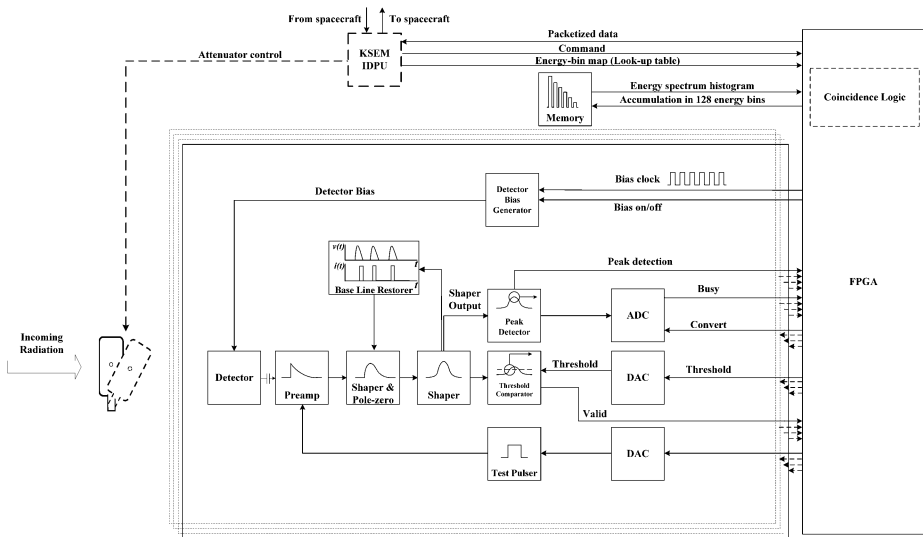


Fig. 7 Functional block diagram of PD signal processing electronics. Each telescope has four chains of signal processing electronics that consists of a series of Multi-Feed Back (MFB) filters, pole-zero cancellation circuit and a Sallen-Key filter along with a BaseLine Restoration (BLR) circuit for high-count rate events

detector stacks to achieve a reduction of particle fluxes by a factor of ~ 70 . The threshold values above and below which the attenuator of the telescope can be rotated into and out of the FOV of the PD, respectively, can be set by tele-commands from the ground. The attenuator can also be rotated to prevent direct sunlight from overheating and damaging the detectors. During summer and winter, direct sunlight can irradiate the PD3 detectors because the FOV is near the ecliptic plane, as demonstrated in Fig. 5. The attenuator of PD3 can be closed with a tele-command from the ground to prevent PD3 from directly viewing the sunlight by specifying the periods of sunlight exposure in a year.

2.3 Signal Processing

Each telescope of the PD employs a set of traditional signal processing chains, as illustrated in Fig. 7. If a charged particle is detected by one of the detectors, the signal is converted into a voltage signal with an Amptek A250F charge-sensitive preamplifier that is placed adjacent to the detector within the sensor head. The signal is then transmitted with coaxial cables to a corresponding signal processing chain for further amplification and shaping. Each pair of a detector and charge-sensitive preamplifier is connected to its own independent signal chain, resulting in a set of four signal chains corresponding to the O, U, T and F detectors of each telescope. The signal from the charge-sensitive amplifier becomes amplified and shaped with a series of Multi-Feed Back (MFB) filters, pole-zero cancellation circuit and a Sallen-Key filter. The shaped pulse from this circuitry is a unipolar Gaussian pulse in the time domain with a peaking time of $2.5 \mu\text{s}$ that allows high-count rate measurements. The baseline of the signal chain is maintained through a BaseLine Restoration (BLR) circuit to acquire accurate measurements of the energy spectrum during high-count rate events.

The minimum voltage value for signal processing is determined by a comparator, of which one input is a programmed value set by a Digital-to-Analog Converter (DAC) circuit.

Table 3 List of valid coincidence logics and their corresponding energies. These valid logics are allocated with energy bins for later summation to calculate energy spectra of electrons and ions. Other combinations of coincidence logics are possible, but those considered invalid are given only with counters for monitoring purposes, but are not resolved in energy. The actual allocation of energy bins can be found in Table 4

Coincidence logic	Electron energy (keV)		Ion energy (keV)	
	F-side	O-side	F-side	O-side
F	100–600	–	350–600	–
FT	400–1500	–	×	–
FTU	1400–2400	–	×	–
FTUO	2200–3800	–	×	–
OUT	–	×	–	19500–22500
OU	–	×	–	6000–19500
O	–	350–2000	–	148–6000

Therefore, only shaped detector signals above a preset voltage level are allowed for subsequent data processing by triggering a valid logic. This valid logic, together with timing information regarding voltage peak occurrence, initiates a calculation of pulse-height analysis by a Field Programmable Gate Array (FPGA). The FPGA controls the associated signal logics, registers event coincidences from multiple detectors, and cumulates counts in a set of pre-programmed energy bins to generate energy spectra of incoming radiation. Each signal processing channel has a test pulser with programmable amplitudes. The test pulser is used to verify the functionality of the instrument in the absence of radiation on the ground. The test pulser can also be used in-orbit as a periodic test method to confirm that the gain and baseline of each channel remain the same or change over the mission lifetime. It should be noted, however, that the test pulser itself may not be used to detect changes in overall PD calibration because the detectors are not involved in running the test pulser.

There is a total of 128 energy bins per telescope, or 256 per PD. According to the combination of coincidence logics simultaneously triggered by each signal processing chain, the detector events are categorized and stored in the energy bins. In general, the expected combination of coincidence logics depends on the species and energy of the incident particles, but the presence of the physical interaction of the particles with surrounding structures of the detector or sensor head may result in unexpected combinations of the coincidence logics. For example, if a low-energy electron is incident, the expected coincidence logic is ‘F’ triggered only by the F detector. A multiple coincidence logic of ‘FT’ is expected with a higher-energy electron if the energy of incident electron is sufficient to penetrate the F detector and deposit a portion of its energy onto the T detector. Similarly, ‘FTU’ and ‘FTUO’ logics are possible with increasing energies of electrons. However, if an electron is multiply scattered, it now becomes possible to have a combination of coincidence logics that does not coincide with a “clean” trajectory. For instance, if a high-energy electron first deposits energy onto the F detector and thus is scattered by the F detector, additionally scattered by any surrounding structure, and finally absorbed by the U detector, a coincidence logic of ‘FU’ is registered, which is not considered valid in the accumulation of energy histograms.

A list of coincidence logics that are considered valid by the FPGA of PD is provided in Table 3. The energy ranges corresponding to the coincidence logics, taking into account the details of the detector responses, are given in the table. The deposited energies for the coincidence logics are calculated with GEometry ANd Tracking 4 (GEANT4, Agostinelli et al. 2003; Allison et al. 2006) Monte-Carlo simulation based on the probabilistic occurrence of

physical interactions of the incident particles. The results of the GEANT4 calculations allow for tailoring of the energy ranges to allocate energy bins to the processed signals. A detailed description of the GEANT4 calculation and the results are provided in Sect. 3.1.

Note that Table 3 does not include combinations of logics that are considered invalid, such as ‘FU’ in the aforementioned paragraph, ‘OT’, ‘FTO’, ‘OUF’ or ‘UT’, that could be triggered by penetration, scattering or simultaneous occurrence of multiple events. For those events related to the coincidence logics other than those listed in Table 3, a small number of counters are reserved in energy bins for the purpose of housekeeping monitoring, but these events are not resolved in terms of the energies. In the flight operation mode of KSEM PD, there are 128 bins allocated to each of the telescope that includes different combinations of valid coincidence logics. All the 128 bins per telescope or 256 per PD are transmitted to the ground from the spacecraft. These bins are then further summed over the coincidence logics from the F-side and O-side events by ground processing, taking into account overlapping energy ranges among the logics, as illustrated in Table 4. The summation yields 48 energy bins available for F-side events and 22 for O-side events. Each energy bin accumulates events corresponding to the energy range from the value indicated in each bin to the value in the next bin. These energy bins are programmable with commands from the ground. Currently, there are more energy bins allocated for F-side (electrons) than O-side (ions) events because the geosynchronous orbits are mostly positioned in the outer electron belt. O-side events are binned with coarser energy resolutions to monitor Solar Energetic Particles (SEPs) events or excursions to the bow shock outside the magnetopause when the magnetosphere is strongly compressed in response to varying solar wind conditions.

3 Numerical Modeling and Calibration

3.1 GEANT4 Simulation

The response function of PD detectors is estimated with the GEANT4 (Agostinelli et al. 2003; Allison et al. 2006) toolkit in this paper. From the general relation between the incident differential particle flux and the detector count rates, the detector count rate in the i th energy bin is related to the incident differential particle spectrum $J(E, \Omega)$ by the following relation (Berger et al. 1969):

$$C_i = \int R_i(E, \Omega) J(E, \Omega) dE d\Omega \quad (1)$$

Here, $J(E, \Omega)$ is the differential particle flux in units of $1/(\text{area} \cdot \text{solid angle} \cdot \text{energy} \cdot \text{time})$, $R_i(E)$ is the response function of the detector that represents the probability of an incident particle of energy E in the direction Ω depositing energy in the i th energy bin. For convenience, we will express the particle flux in units of $1/(\text{cm}^2 \text{sr keV s})$ in this paper. The response function $R_i(E)$ characterizes the pulse-height spectrum of the detector and represents how the detector system accumulates counts in energy bins in response to the incident particles of kinetic energy E and incident angle Ω . The simplifying assumption of isotropic flux of $J = J(E)$ and discretization of the response function over the measurable energy ranges of detectors yields the following matrix relation between the counts and differential fluxes:

$$C_i = \sum_j R_{ij} J_j \Delta E_j \quad (2)$$

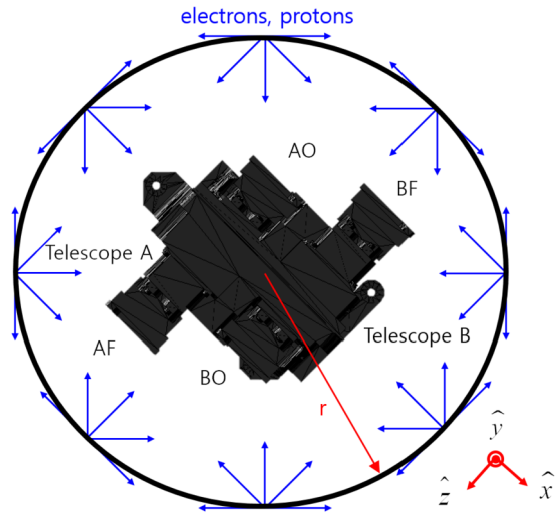
Table 4 Nominal flight energy bins for KSEM PD. Each energy bin accumulates events

corresponding to the energy range from the value indicated in each bin to the value in the next bin. The energy bins are programmable with commands from the ground. Currently, there are more energy bins allocated for F-side (electrons) than O-side (ions) events according to a consideration that the geosynchronous orbits are mostly positioned in the outer electron belt. O-side events are binned with coarser energy resolutions to monitor Solar Energetic Particles (SEPs) events or excursions to the bows shock outside the magnetopause when the magnetosphere is strongly compressed in response to the varying solar wind conditions

Bin no.	Energy (keV)	Bin no.	Energy (keV)	Bin no.	Energy (keV)
F-side event energy bins					
1	100	21	800	41	2200
2	125	22	850	42	2400
3	150	23	900	43	2600
4	175	24	950	44	2800
5	200	25	1000	45	3000
6	225	26	1050	46	3200
7	250	27	1100	47	3400
8	275	28	1150	48	3600
9	300	29	1200		
10	325	30	1250		
11	350	31	1300		
12	375	32	1350		
13	400	33	1400		
14	450	34	1500		
15	500	35	1600		
16	550	36	1700		
17	600	37	1800		
18	650	38	1900		
19	700	39	2000		
20	750	40	2100		
O-side event energy bins					
1	148	11	1308	21	21000
2	185	12	1626	22	>22500
3	229	13	2021		
4	285	14	2513		
5	354	15	3123		
6	441	16	3883		
7	548	17	4827		
8	681	18	6000		
9	846	19	9500		
10	1052	20	11000		

where $J_j \Delta E_j$ is the integral particle flux, i.e., fluence, over the j th energy bin of $J(E)$ in the energy range $(E_j, E_j + \Delta E_j)$. The response matrix R_{ij} has units of $\text{cm}^2 \text{sr}$ and accounts for the pulse-height spectrum of detector counts over the energy bins. The response matrix R_{ij} is upper-triangular as the incident particles may deposit only a portion of incident energies to the detector, thus generating detector counts in lower energy bins. In this study, isotropic fluxes of electrons and protons are produced from the surface of a hypothetical sphere, as illustrated in Fig. 8 (Yando et al. 2011). In this simulation, PD is surrounded by a hypothetical shooting sphere on which charged particles are injected inward to calculate the response function of PD. The energy distributions of the incident particles are in uniform logarithmic scales of 10 keV–10 MeV for electrons and 10 keV–50 MeV for protons (Pak

Fig. 8 Calculation of the PD response function with GEANT4. A hypothetical sphere surrounding the PD injects charged particles inward to simulate isotropic fluxes. The detector accumulates the number of counts in the deposited energy bins as a function of incident energy bins for estimation of the response matrix



et al. 2018). The response matrix R_{ij} under the isotropic flux over the full 4π steradians of space is calculated according to the following relation:

$$R_{ij} = \frac{n_i}{J_j} \tag{3}$$

Here, J_j is the generated flux of simulated particles in the j th energy bin and n_i is the accumulated count of simulated hits on the detector in the j th bin. If the total number of incident particles over the j th energy bin is N_j and the area of particle generation is the surface of a hypothetical sphere of radius r , Eq. (3) is converted into the following form:

$$R_{ij} = \frac{n_i}{N_j} 4\pi^2 r^2 \tag{4}$$

The response matrices as derived from the GEANT4 simulations are shown in Fig. 9 for all of the F-side and O-side events with respect to the incident ions and electrons. The figure illustrates response matrices, taking into account all of the coincidence logics, for both the F-side events and O-side events with respect to electrons and protons. The absolute magnitudes of the response matrices are color-coded according to the color bar on the right-hand side of each figure. Each figure shows the response of detectors as a function of incident energies for the events triggered by the F- or O-side of the telescope for electrons or protons, respectively. For example, Fig. 9(a) represents the F-side detector’s response generated by electrons, taking into account all of the valid coincidence logics of ‘F’, ‘FT’, ‘FTU’ and ‘FTUO’. The horizontal axis in the figure is the incident energy, whereas the vertical axis is the deposited energy. Along the diagonal of the figure is the detector response for the case of a total transfer of particle energy, i.e., deposited energy equals incident energy. The response below the diagonal line is the detector response for a partial transfer of incident energy for which deposited energy is smaller than the incident energy. Therefore, a vertical column of the detector response in the figure should represent each pulse-height spectrum of the detector for a given incident energy. Note that Figs. 9(a) and 9(d) are the primary responses of the PD telescope, F-side response by electrons, and O-side by protons. On the other hand, Figs. 9(b) and 9(c), which represent the detector responses for the F-side by

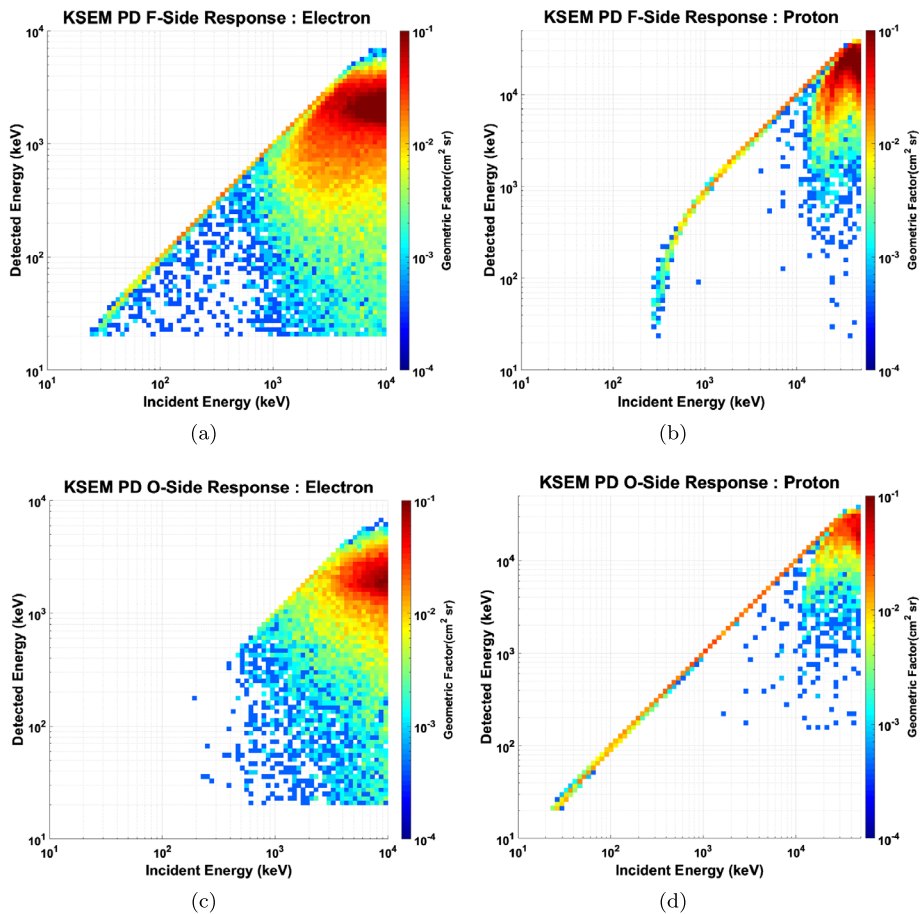


Fig. 9 Response matrices as derived from GEANT4 simulations when the attenuator is open. The magnitudes of response functions are color-coded according to the color bar shown on the right-hand side of each plot. Along the diagonal of the figure is the detector response for the case of a total transfer of particle energy for which deposited energy equals incident energy. F-side responses of the PD with respect to electrons and protons are shown in plots (a) and (b), whereas O-side events are shown in plots (c) and (d). Plots (a) and (d) are the primary responses of the PD telescope, F-side response by electrons and O-side by protons. On the other hand, plots (b) and (c) can be considered as contamination by other ion species. Plots (b) and (c) show that protons and electrons are effectively blocked for energy below 350 keV due to foils and magnetic fields, respectively

protons and the O-side by electrons, can be considered as contaminated by other ion species. In Fig. 9(b), the F-side response by protons is clearly eliminated below ~ 350 keV due to the thin foil in front of the F detector, as explained in Sect. 2.2. It is also shown in Fig. 9(c) that the response of O-side by electrons is clearly diminished below ~ 350 keV due to magnetic fields that sweep away low energy electrons. All the plots show strong responses at high energies, above ~ 2 MeV for electrons and above ~ 20 MeV for protons, because of direct penetration through the mechanical structure of sensor housing.

It is often convenient to express the detector responses by integrating over all the deposited energies as a function of incident particle energy and call it an effective geometric factor. The effective geometric factor is a simplification of the complicated detector response

function and is calculated by integrating over the energy spectrum of deposited energies in the detectors. In a discretized form, the effective geometric factor corresponding to the detected energy range of the i th bin is obtained by summing all the elements of the i th column space of the response function matrix in Eq. (4). The energy-dependent geometric factor represents a probability that the detector accumulates counts irrespective of the deposited pulse-height spectrum as a function of the incident particle energy. In Fig. 10, the effective geometric factor of the PD is summarized. On the left-hand side of the figure, the effective geometric factors for each of F, FT, FTU and FTUO events are provided for both the electron and ions. The bottom plot is the sum of all the responses from these four coincidence events. In a similar manner, the geometric factors for each of O, OU, OUT and OUTF events are given on the right-hand side with the bottom plot again as a sum of all the four events. In the figure, the horizontal dashed line is a theoretical geometric factor of the detector response, $0.02 \text{ cm}^2 \text{ sr}$, based on an assumption of straight particle trajectories without any scattering or penetration (Sullivan 1971). The top plots, Figs. 10(a) and 10(b), demonstrate that the single coincidence logics F and O primarily correspond to the detection of electrons (in blue) and protons (in red), respectively, with a clear separation of electrons and protons in the energy range below $\sim 350 \text{ keV}$. The vertical error bars in each plot represent uncertainties of the Poisson statistics from the GEANT4 simulation. However, the responses of electrons and protons for the F-event, as shown in Fig. 10(a), are comparable in the energy range of about $350\text{--}800 \text{ keV}$, which indicates that the proton contamination in the electron measurement can be substantial. On the other hand, the responses are more distinct for the O-event, shown in Fig. 10(b), between the electrons and protons in the same energy range. Therefore, reference to the O-event should provide a clue to a proper interpretation of the F-event in terms of electron events. If there is a weak response from the O-event in the energy range of about $350\text{--}800 \text{ keV}$, the contamination of the F-event by protons should be low since the detector response for the O-event is significantly more sensitive to protons than electrons in this energy range.

The rapid increases of electron and proton responses above $\sim 2 \text{ MeV}$ and $\sim 20 \text{ MeV}$, respectively, are due to the penetration of high-energy particles through the structures of sensor-head housings. Electrons and protons with these energies can penetrate effective aluminum thicknesses of $\sim 2 \text{ mm}$, which is roughly consistent with the thickness of the thin section of the sensor head. The geometric factors for the detection events corresponding to multiple logics are shown in Figs. 10(c)–10(h) for F-side and O-side events, respectively. The plots generally demonstrate that the responses of electrons and protons for each multiple-logic event are distinct from each other in terms of their incident energies.

It should be noted that the observed count from the detector is a convolution of detector responses with input particle fluxes. Estimation of particle fluxes (input) based on the observed counts (output) belongs to a category of inverse problem that is not covered in this paper. However, because previous observations of charged particle fluxes in geostationary orbits are numerically available, it is possible to quantitatively estimate the anticipated amount of cross-contamination of the F-side and O-side measurements based on the average and extreme cases of charged particle fluxes in the geostationary orbits. These results are provided in Sect. 3.3.

3.2 Calibration

The relationship between the energy deposited in the detector and the digitized height of the shaped pulse in terms of the ADC value is derived considering various radioisotopes of well-known energies. There are three radioisotopes used in the present study: ^{241}Am , ^{109}Cd

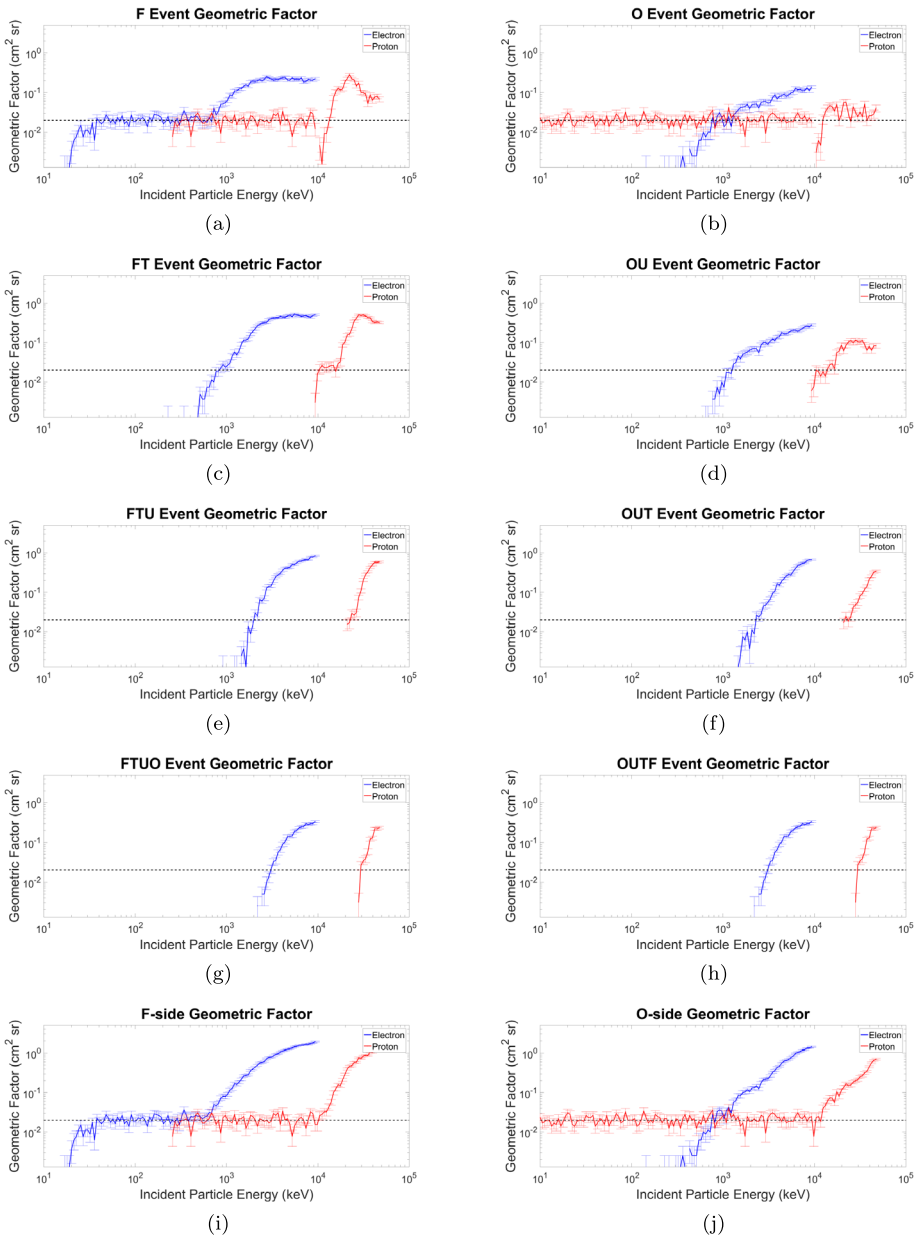


Fig. 10 Effective geometric factors of the PDs. The effective geometric factor is a simplification of the detector response function and is obtained by integrating over the entire deposit energy spectrum of incident particle beams. The geometric factors for each coincidence event are separately shown in the top four rows for both protons and electrons. The fifth row is a plot of the total geometric factor for all coincidence events. The horizontal dashed line in each plot is a theoretical geometric factor of $0.02 \text{ cm}^2 \text{ sr}$ that is obtained with an assumption of straight particle trajectory without any scattering or penetration (Sullivan 1971)

Table 5 Radioisotopes and their photon emission energies used in the determination of energy-channel relationships for PDs

Radioisotope	Photon energy
^{241}Am	59.6 keV
^{109}Cd	88.0 keV
^{57}Co	122.1, 136.5 keV

and ^{57}Co . Four emission lines of photons in Table 5 generated from these isotopes are used to calibrate energy relative to the digitized values from the signal processing electronics. It is noted that the absence of electric charge for photons allows interactions only through the photoelectric effect, Compton scattering and pair production. A photon that interacts with the silicon detector through these processes is completely removed from the incident beam, but it is not degraded in terms of energy, only attenuating in terms of intensity. The photon interaction is considerably different from those of charged particles, such as electrons or ions, which undertake numerous small-angle scatterings with a target material. Therefore, with a small cross section for all the processes, photons are far more penetrating than charged particles, allowing calibration of not only the F and O detectors positioned outside, but also the thick U and T detectors located inside the detector stacks of the PD.

In the energy-channel calibration of flight model PDs, a separate Look-Up Table (LUT) utilizing the finest energy bins available in a limited energy range of interest is applied to each detector under calibration. This LUT used in the energy-channel calibration is different from the in-orbit LUT in Table 4 and is used only for the ground calibration for accurate determination of deposited energy as a function of the digitized values of pulse peaks according to the descriptions in Sect. 2.3. Figure 11 shows the responses of the flight models PD1, PD2 and PD3 relative to the four emission lines. Each peak represents a response from the detectors relative to incident photons of known energies and is fitted with a Gaussian distribution. The Gaussian fit yields two parameters for subsequent analyses, the digitized value from ADC for each peak and associated Full-Width-at-Half-Maximum (FWHM), which is considered as a variance of the pulse height distribution. The results of Fig. 11 show that there are differences in the final pulse height distributions among the detectors. Identification of pulse height peaks relative to the emission lines can be obscure due to various factors affecting the final performances of detectors, including noise levels, gains and efficiencies of the detectors. If the peaks are not identified definitively, the data are not considered for the Gaussian fit. A least-square fit is then performed in Fig. 12 between the known energies and the ADC values for each peak estimated from the Gaussian fit. In the figure the error bars of data points are the same as the FWHMs determined from the results of Fig. 11. The least-square fit yields two parameters, gain and offset, for a linear relation between the estimated energy and the digitized value of the peak through the relation $\text{Energy} = \text{Gain} \times \text{ADC value} + \text{Offset}$. The parameters as determined from the least-square fit for each detector of the telescopes are tabulated in Table 6. Note that the uncertainties for the U and T detectors are relatively large compared to the rest of the detectors because of broader variances from the FWHM of the identified peaks.

3.3 PD Count Rates with Model Fluxes

For a quantitative assessment of the expected count rates and cross-contamination in the detected events, model fluxes of electrons and protons are convoluted with the detector responses from the GEANT4 simulation. For electron fluxes in geosynchronous orbit, the IGE2006 model (Sicard-Piet et al. 2008) is employed, whereas AP-8 (Sawyer and Vette

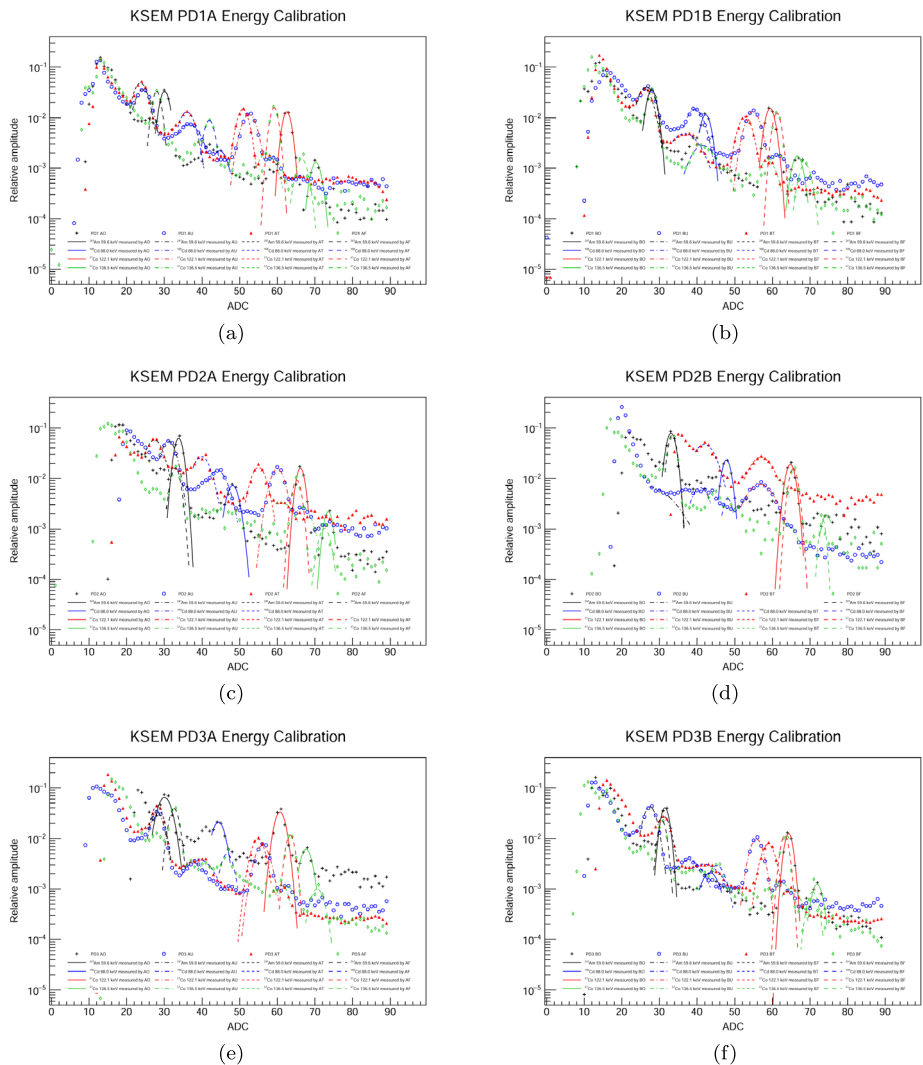


Fig. 11 The response of flight models PD1, PD2 and PD3 acquired during energy-channel calibration. Each telescope is exposed to ^{241}Am , ^{109}Cd and ^{57}Co to determine digitized peak values of signal pulses in terms of known energies. The response of the telescope to emitted photons from the radioisotope is fitted with a Gaussian distribution to determine the peak and a Full-Width-at-Half-Maximum (FWHM). The ordinate represents the measured count rates in an arbitrary scale

1976) is used for proton fluxes. These model fluxes are calculated through an online service provided by SPENVIS (Heynderickx et al. 2000) and are illustrated in Fig. 13. The electron fluxes are calculated for the cases of upper, average and lower fluxes that could be encountered during solar cycles for years relative to the solar minimum. For protons, AP-8 (Max) and AP-8 (Min) are calculated, but they are practically the same for geostationary orbits. An extreme case of energetic solar proton event is modeled with CREME-96 (Peak 5-min) model (Tylka et al. 1997). Note that these models only represent limited aspects of truly dynamic variations of charged particle populations in the geostationary orbits. Therefore,

Fig. 12 Least-square fit between the energies of the radioisotopes and the digitized values of the peaks is performed assuming a linear relation. The horizon error bar of each data point is derived from the FWHM from the results of Fig. 11

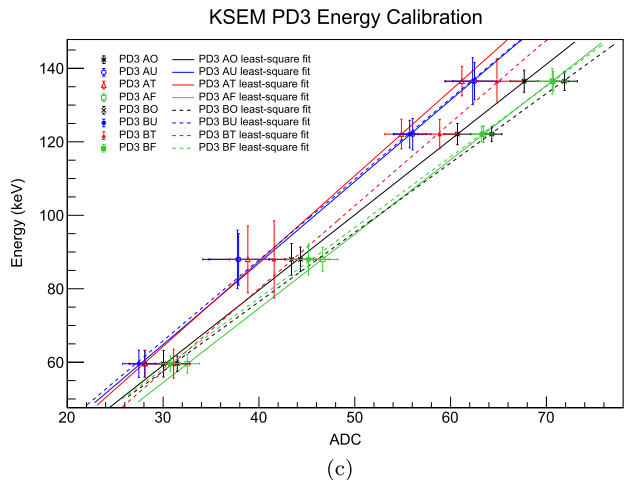
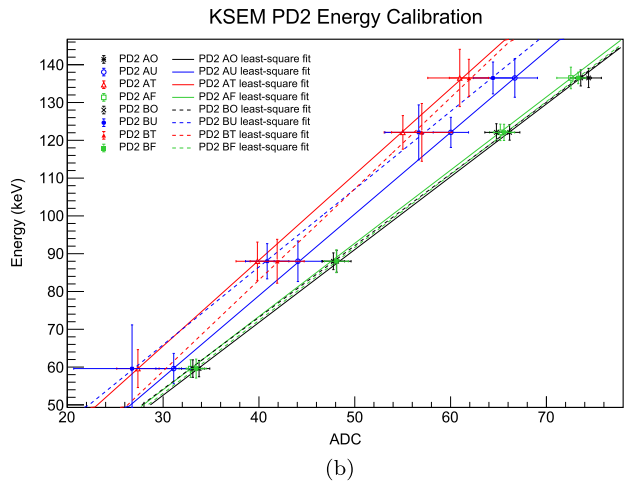
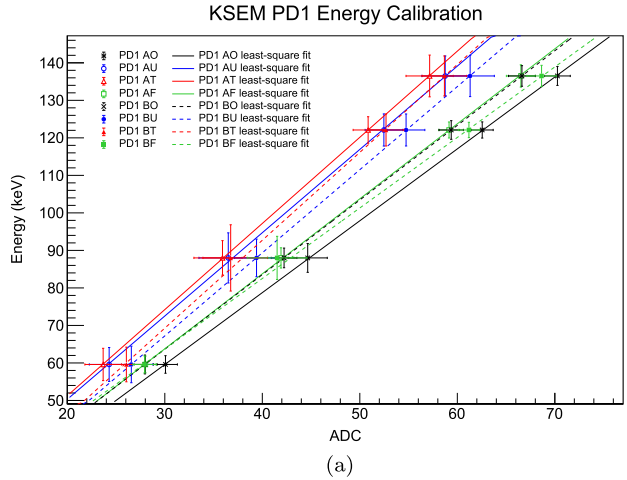
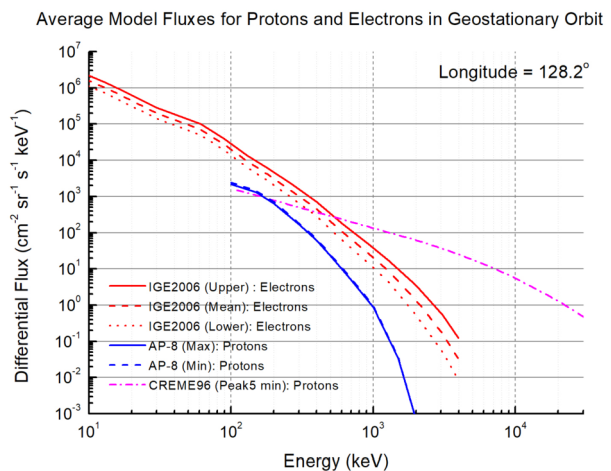


Table 6 Results of linear least-square fit for digitized peak values of PD1, PD2 and PD3 relative to known energies from radioisotopes. Estimate of deposited energy is related to the obtained gain and offset through a linear relation, i.e., Energy = Gain × ADC value + Offset. Uncertainties of the derived parameters from the least-square fit are shown in parentheses

Detector	Gain	Offset
PD1 AO	1.92 (±0.08)	2.11 (±4.30)
PD1 AU	2.22 (±0.18)	5.90 (±8.04)
PD1 AT	2.30 (±0.17)	5.34 (±7.51)
PD1 AF	2.00 (±0.08)	3.80 (±4.05)
PD1 BO	1.99 (±0.09)	3.99 (±4.37)
PD1 BU	2.22 (±0.18)	0.73 (±8.70)
PD1 BT	2.34 (±0.19)	-1.04 (±8.86)
PD1 BF	1.88 (±0.08)	7.32 (±4.11)
PD2 AO	1.93 (±0.07)	-5.25 (±4.10)
PD2 AU	2.16 (±0.16)	-7.45 (±8.11)
PD2 AT	2.27 (±0.21)	-2.58 (±9.61)
PD2 AF	1.94 (±0.08)	-4.07 (±4.74)
PD2 BO	1.90 (±0.07)	-2.83 (±4.18)
PD2 BU	2.06 (±0.23)	4.10 (±12.52)
PD2 BT	2.42 (±0.42)	-13.79 (±23.48)
PD2 BF	1.93 (±0.06)	-4.88 (±3.61)
PD3 AO	2.05 (±0.11)	-2.33 (±6.21)
PD3 AU	2.22 (±0.16)	-1.88 (±7.22)
PD3 AT	2.32 (±0.15)	-5.42 (±7.39)
PD3 AF	2.02 (±0.09)	-6.17 (±5.10)
PD3 BO	1.89 (±0.07)	0.75 (±3.98)
PD3 BU	2.20 (±0.16)	-0.21 (±7.48)
PD3 BT	2.26 (±0.17)	-10.32 (±8.63)
PD3 BF	1.92 (±0.07)	0.52 (±3.93)

Fig. 13 Average proton and electron fluxes based on models in geostationary orbit. For electron fluxes in geosynchronous orbits, the IGE2006 model (Sicard-Piet et al. 2008) is employed, whereas AP-8 (Sawyer and Vette 1976) is used for proton fluxes. An extreme case of an energetic solar proton event is modeled with the CREME-96 (Peak 5-min) model (Tylka et al. 1997)



the calculations below may serve as case studies of various probable occasions, but should not be considered to generally refer to the detector performance. Great caution needs to be exercised case by case for a reasonable understanding of each observation.

Based on the model fluxes, estimated count rates of the PD are shown in Fig. 14. Each plot shows the total counts expected from the incident proton and electron fluxes convoluted with response matrices derived from the GEANT4 calculations in Sect. 3.1. There are three cases considered: the average case, the upper case, and an extreme case, which is expected only during intense events of solar energetic particles. In the top row, the count rates are shown for IGE2006 (mean) and AP-8 (min) fluxes. Similar calculations with model fluxes for IGE2006 (upper) and AP-8 max are in the second row. The count rates for each energy bin are plotted according to the scale on the left-hand side, whereas cross-contamination of the estimated count rates, F-side by protons and O-side by electrons, are quantified according to the scale on the right-hand side in terms of a percentage of the total count rates. These results show that the contamination due to protons in the F-events are small on average. In the limited energy range of about 300–600 keV the proton contamination is increased, but it is generally less than $\sim 10\%$. The possibility that this energy range may be contaminated by the proton fluxes has been previously identified with the effective geometric factor in Sect. 3.1. This relatively small contribution of protons in the F-event counts is owing to the fact that in geosynchronous orbits, the proton particle fluxes are significantly smaller. On the other hand, the electron contribution to the O-side events is not negligible above the range of ~ 350 keV, as illustrated on the right-hand side of Fig. 14. These results may seem contradictory to the previous findings from Sect. 3.1, where it is noted that the response of O-event is considerably more insensitive to the electrons than protons in the energy range of this contamination. This is again due to the fact that at the geostationary orbit, electron fluxes are usually an order of magnitude higher than the proton fluxes: the higher fluxes of electrons convoluted with the smaller detector responses can yield considerable count rates for O-events above ~ 350 keV. The results shown in Figs. 14(b) and 14(d) suggest that great care must be exercised in interpreting the O-event in terms of proton fluxes. Under usual cases of proton and electron fluxes that are close to those with model fluxes, O-events up to only about 350 keV should be interpreted as proton events.

The detector responses for the case of extreme solar particle fluxes, as estimated with CREME96 (peak 5-min) for protons, are shown in the bottom row of Fig. 14. The previous conclusion of small contamination of the F-side events by protons is no longer valid with the model. In this extreme case of proton fluxes in the geosynchronous orbit, the detector counts are dominated by incident proton fluxes. The majority of O-side events are accounted for with protons, whereas the electron contribution for the total counts of the O-side events are minimal. On the other hand, protons are responsible for a significant portion of F-side events under 600 keV, as shown in the figure. For the result of Fig. 14(e), it is noted that the abrupt decrease of proton contribution in the F-side events above 600 keV is an artifact of allocating energy bins for the F-detector only for energies up to 600 keV. The F-detector is primarily intended for the detection of electrons, which are capable of depositing energy of no more than 600 keV over a 675- μm -thick detector. Therefore, there are many energy bins allocated below 600 keV for electrons, as tabulated in Table 4, but the bin allocation is not extended above 600 keV. Only a total sum of all counts above 600 keV is stored in a single bin without any energy resolution. Any protons above 600 keV, such as those modeled with the CREME96, will be counted in this single bin for the F events.

4 Flight Operation and Data

The GEO-KOMPSAT-2A (GK2A) spacecraft carrying KSEM as a secondary payload was launched into a parking orbit with Ariane-5ECA on December 4, 2018. After a few orbit maneuvers, the spacecraft arrived at the geostationary orbit with a final longitude of 128.2°E,

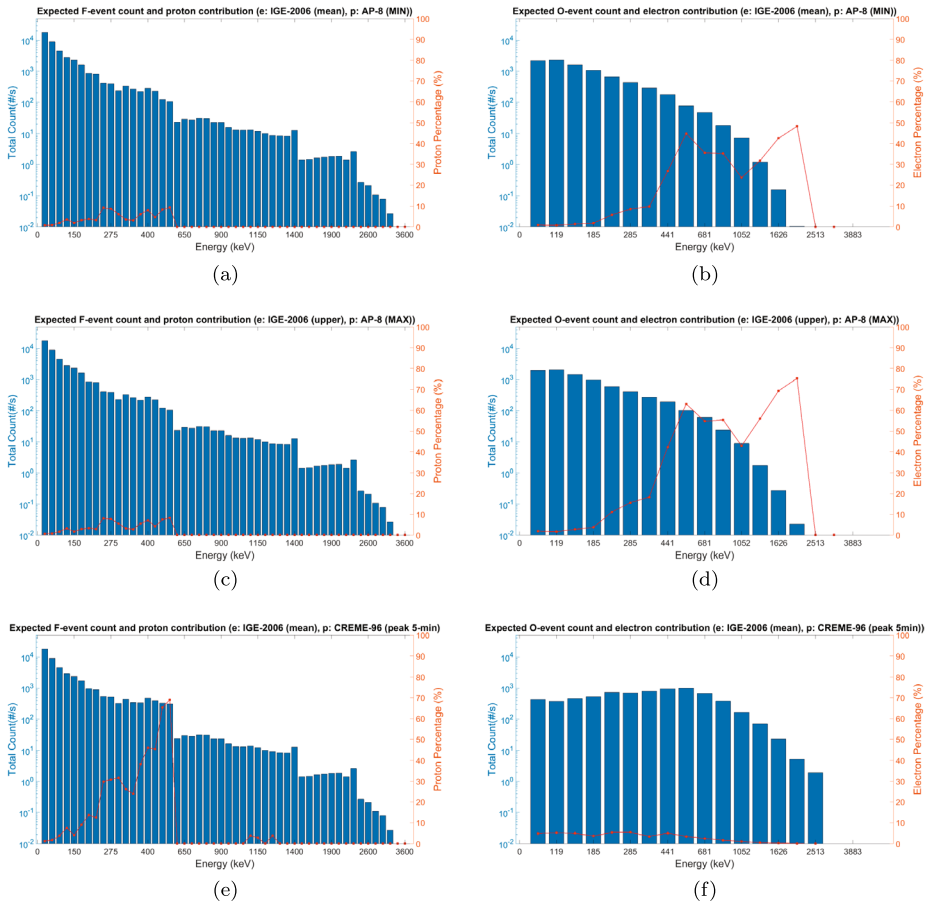


Fig. 14 Expected count rates of the PD based on numerical flux models of the protons and electrons in geosynchronous orbits. The count rates are estimated with IGE2006 (mean) for electron fluxes and AP-8 (min) for protons in plots (a) and (b), IGE2006 (upper) and AP-8 (max) in plots (c) and (d), and IGE2006 (mean) and CREME-96 (peak 5-min) in plots (e) and (f). Detector responses of the F-side events for each case are shown on the left-hand side, whereas responses of the O-side events are shown on the right-hand side. Red lines in each plot represent the percentage of bin count rates due to protons for F-side events and electrons for O-side events, according to the scale on the right side of the figure. Under the average fluxes of electrons and protons, the contamination of F-side events due to protons is generally less than $\sim 10\%$. However, the contamination of O-side events due to electron fluxes could be significant above 350 keV. Under the extreme case of solar proton events, all the O-side events are dominated with incident solar protons, whereas F-side events are severely contaminated by the protons, as shown in plots (e) and (f)

an inclination of 0° and a mean orbital radius of $6.6 R_E$ by the end of year 2018. The commissioning of the KSEM instrument began on January 4, 2019 and lasted until the end of June 2019. The commissioning activities of the KSEM instrument included adjustments of detector baselines and low-level discriminator levels in the signal processing electronics of PD1, PD2 and PD3. All the housekeeping telemetry is currently within the normal ranges and are consistent with those measured on the ground acquired during environmental tests of the instrument. The KSEM instrument is being operated in normal mode after successfully having accomplished initial power-on of the instrument and commissioning activities

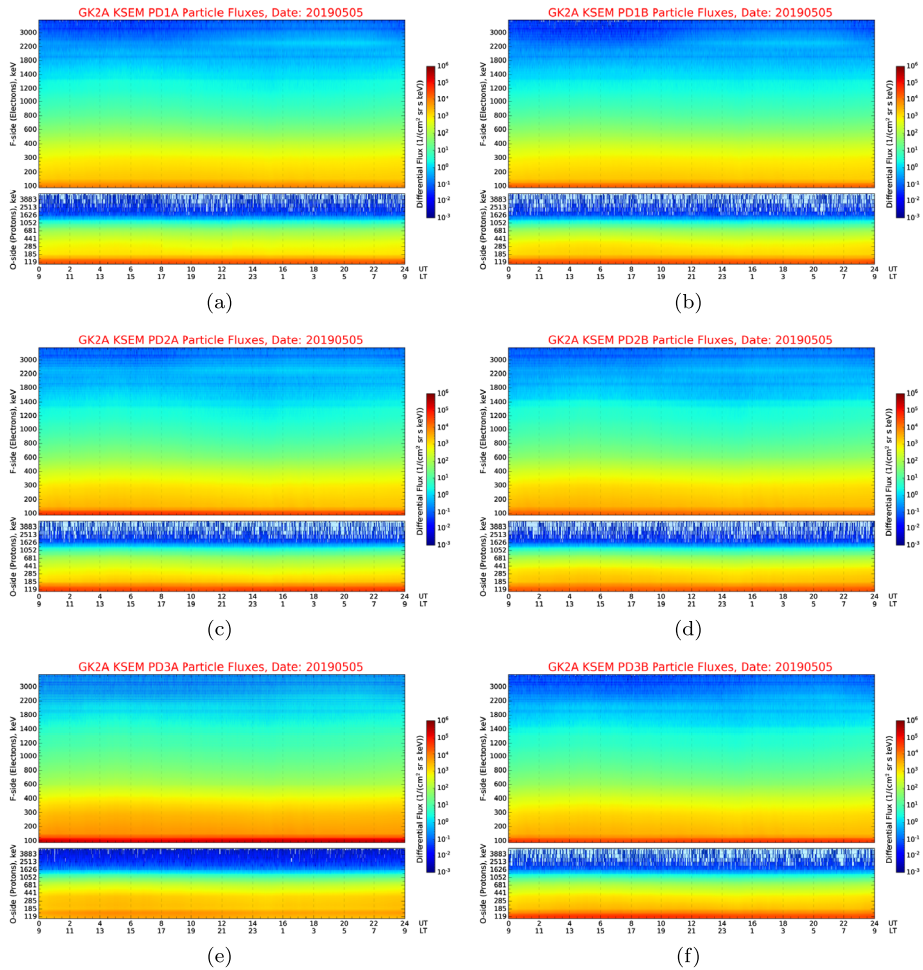


Fig. 15 Differential fluxes with KSEM PD1, PD2 and PD3 on 5 May 2019. The fluxes are color-coded according to the color-bar shown on the right-hand side. All the measurements from six telescopes are shown from plots (a) to (f). In each plot, F-side measurements, interpreted as electron events, are shown at the top and O-side, as ions, bottom. During the day, the D_{ST} and K_p index remained low, indicating a quiet magnetosphere. The KSEM measurements in the outer radiation belt also clearly show that there were no significant variations for both the electron and ion fluxes

specific to each sensor. The downlink of KSEM data, including all of the housekeeping telemetry and science data, are maintained continuously without any interruption within a bandwidth of 19.2 kbps. The telemetry and science data are accumulated over one second and periodically transmitted to Earth, also once per second. In consideration of the limited downlink speed of 19.2 kbps, each PD is cyclically polled once per second by the instrument electronics, resulting in 3-s cadence for each PD in normal operation mode.

In Fig. 15, the differential fluxes of electrons and protons as estimated with detected counts according to the energy bins in Table 4 are provided for the day of 5 May 2019. On that day, the outer radiation belts remained relatively quiet, without significant variations of proton and electron fluxes. The hourly average of Disturbance Storm Time index (D_{ST})

and three-hour planetary K index (K_p) remained relatively low, $-17 \text{ nT} < D_{st} < 3 \text{ nT}$ (data from World Data Center for Geomagnetism, Kyoto) and $K_p < 1+$ (data from the Helmholtz Centre, Potsdam). The differential fluxes are estimated with the energy-dependent geometric factors shown in Fig. 10. The fluxes are currently estimated with an assumption of no significant cross-contamination between the F-side and O-side events. Such assumptions only provide results with restricted validity. Further analyses are being undertaken to more accurately estimate the fluxes, taking into account the available numerical methods such as forward fitting or regularization from the inverse theory. These are the subjects of further investigations and are not treated in this paper. The results shown in this paper should be considered as a first-cut from the early operations, with more refined results soon to come in subsequent investigations. The differential fluxes in Fig. 15 for electrons and protons from all six telescopes are color-coded according to the color bar on the right-hand side of each plot. All of the telescopes generally show a similar trend of no significant flux variations during the day, while clearly demonstrating the capabilities of KSEM PD with excellent energy resolution, especially for the electron measurements with F-side events.

In Fig. 16, the differential fluxes of electrons and protons are shown for the day of 11 May 2019. The geomagnetic indexes of D_{st} and K_p for this day were in the range of $-21 < D_{st} < -51 \text{ nT}$ and $K_p < 5^\circ$, indicating a moderately disturbed magnetosphere. All responses from PD1, PD2, and PD3 generally show that there has been a significant increase of relativistic electron fluxes after $\sim 1400 \text{ UT}$, whereas such relativistic fluxes, especially in the energy range above $\sim 800 \text{ keV}$, were not present before $\sim 1400 \text{ UT}$. It is also noteworthy that different dynamics of ions and electrons are observed near 0210, 0830 and 1215 UT. For these measurements, the ions below $\sim 300 \text{ keV}$ are observed first, followed by observations of electrons below $\sim 300 \text{ keV}$. There exists a definite timing difference between the ions and electrons with the ions preceding electrons by at least a few minutes in the observation time of the figure. Both the ions and electrons show energy-dependent dispersion, with higher-energy particles arriving earlier. By 2300 UT, all electron measurements of PDs show enhanced fluxes of relativistic electrons extending up to $\sim 3000 \text{ keV}$, which is close to the instrument limit of the energy range for the electron measurements. There were no reports of solar activity on May 11, 2019 and ACE and WIND measurements did not show any increase of energetic electrons or protons indicating PDs likely have measured effects of magnetospheric activities. The Interplanetary Magnetic Field (IMF) B_z component fluctuated before 0800 UT, but subsequently B_z remained southward (-10 nT) until the end of the day. The behavior of PD electrons and protons (Fig. 16) could be associated with three small substorm events on 11 May 2019, with onsets at 02 UT, 09 UT and 12 UT. It is expected that detailed observations of ions and electrons, such as those illustrated in Fig. 16, will allow a quantitative analysis in terms of the adiabatic and non-adiabatic physics of charged particles in the Earth's magnetosphere that will be a significant contribution of KSEM to the physics of space weather at the geostationary orbit from the vantage point of a far-east longitude.

5 Conclusion

The KSEM PD instrument aboard the GK2A spacecraft has been successfully deployed and commissioned to make important observations of charged particle populations at a longitude of 128.2°E in geostationary orbit. These observations, along with measurements of Earth's magnetic fields by SOSMAG, will allow quantitative analyses of particle dynamics. Detailed descriptions of the PD instrument are provided in this paper to show the configuration of the three PD sensors relative to the spacecraft, to explain processing of detector signals,

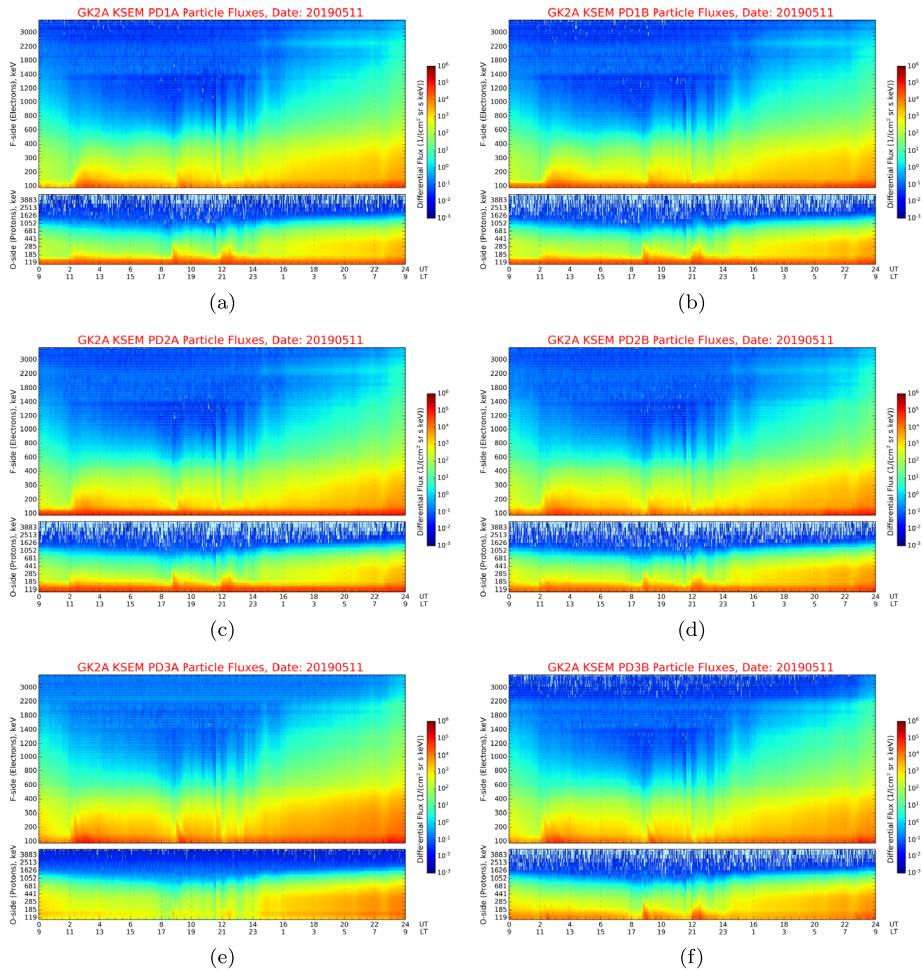


Fig. 16 Differential fluxes with KSEM PD1, PD2 and PD3 on 11 May 2019. During the day, the D_{ST} and K_p indexes were in the range of $-21 < D_{ST} < -51$ nT and $K_p < 5^\circ$, indicating a moderately disturbed magnetosphere. All responses from PD1, PD2, and PD3 generally showed similar features such as increases of relativistic electron fluxes after ~ 1400 UT. Different dynamics of ions and electrons, as observed with all PDs, are also illustrated near 0210, 0830 and 1215 UT when ions below < 300 keV are observed first with O-sides of PDs, followed by electrons with F-sides below < 300 keV. Both the ions and electrons show energy-dependent timing of the events; the higher the energy, the earlier the arrival time. By 2300 UT, all electron measurements show enhanced fluxes of relativistic electrons

and to provide results of instrument performances as estimated via numerical simulation and ground calibration. Representative examples of in-orbit measurements by the three instruments acquired during days of quiet and disturbed geomagnetic periods are shown to demonstrate that the instruments are now successfully operational and able to provide serviceable inputs to space science and space weather communities. The comparison of particle fluxes with those measured by existing or future missions will improve our understanding on the dynamics of charged particles in the Earth’s magnetosphere. It is expected that the KSEM measurements will contribute to a much better understanding on the physics of space weather by adding the vantage point of a far-east longitude in geostationary orbits.

Acknowledgement The authors wish to acknowledge and thank the GK2A project team of Korea Aerospace Research Institute (KARI) for support provided during the integration and testing of the KSEM instrument with the spacecraft. The authors also appreciate support from the National Meteorological Satellite Center (NMSC) of Korea Meteorological Administration (KMA) throughout the project. Findings and opinions included in the present paper should be considered as those assessed by instrument developers and may not necessarily coincide with official opinions and decisions related to the project. Details of the dissemination policy for KSEM data will be prepared and exercised by NMSC. Part of this work was supported by the BK21 plus program through the National Research Foundation (NRF) funded by the Ministry of Education of Korea.

Publisher's Note Springer Nature remains neutral with regard to jurisdictional claims in published maps and institutional affiliations.

References

- S. Agostinelli, J. Allison, et al., K. Amako, J. Apostolakis, H. Araujo, P. Arce, M. Asai, D. Axen, S. Banerjee, G. Barrand, Geant4—a simulation toolkit. *Nucl. Instrum. Methods Phys. Res., Sect. A, Accel. Spectrom. Detect. Assoc. Equip.* **506**(3), 250–303 (2003)
- J. Allison, K. Amako, J. Apostolakis, H. Araujo, P.A. Dubois, M. Asai, G. Barrand, R. Capra, S. Chauvie, R. Chytracsek, Geant4 developments and applications. *IEEE Trans. Nucl. Sci.* **53**(1), 270–278 (2006)
- R.L. Arnoldy, K.W. Chan, Particle substorms observed at the geostationary orbit. *J. Geophys. Res.* **74**(21), 5019–5028 (1969). <https://doi.org/10.1029/JA074i021p05019>
- D. Baker, T. Fritz, B. Wilken, P. Higbie, S. Kaye, M. Kivelson, T. Moore, W. Stüdemann, A. Masley, P. Smith, Observation and modeling of energetic particles at synchronous orbit on July 29, 1977. *J. Geophys. Res. Space Phys.* **87**(A8), 5917–5932 (1982)
- R. Belian, D. Baker, P. Higbie, E.H. Jr, High-resolution energetic particle measurements at 6.6 RE, 2. High-energy proton drift echoes. *J. Geophys. Res. Space Phys.* **83**(A10), 4857–4862 (1978)
- M. Berger, S. Seltzer, S. Chappell, J. Humphreys, J. Motz, Response of silicon detectors to monoenergetic electrons with energies between 0.15 and 5.0 MeV. *Nucl. Instrum. Methods* **69**(2), 181–193 (1969)
- F. Bogott, F. Mozer, Nightside energetic particle decreases at the synchronous orbit. *J. Geophys. Res.* **78**(34), 8119–8127 (1973)
- V. Bothmer, I.A. Daglis, *Space Weather—Physics and Effects* (Springer, Berlin, 2007)
- W. Cummings, P.C. Jr, Magnetic fields in the magnetopause and vicinity at synchronous altitude. *J. Geophys. Res.* **73**(17), 5699–5718 (1968)
- D.A. Gurnett, A. Bhattacharjee, *Introduction to Plasma Physics* (Cambridge University Press, Cambridge, 2005)
- D. Hastings, H. Garrett, *Spacecraft Environment Interactions* (Cambridge University Press, Cambridge, 2004)
- D. Heynderickx, B. Quaghebeur, E. Speelman, E. Daly, ESA's SPace ENVironment Information System (SPENVIS)—a WWW interface to models of the space environment and its effects, in *38th Aerospace Sciences Meeting and Exhibit* (2000), p. 371
- M.G. Kivelson, C.T. Russell, *Introduction to Space Physics* (Cambridge University Press, Cambridge, 1995)
- D. Larson, T. Moreau, Geospace environment modeling (gem) workshop, in *Using the THEMIS Energetic Particle Data* (2009)
- D.E. Larson, R.J. Lillis, C.O. Lee, P.A. Dunn, K. Hatch, M. Robinson, D. Glaser, J. Chen, D. Curtis, C. Tiu, The maven solar energetic particle investigation. *Space Sci. Rev.* **195**(1–4), 153–172 (2015)
- W. Lennartsson, D.L. Reasoner, Low-energy plasma observations at synchronous orbit. *J. Geophys. Res. Space Phys.* **83**(A5), 2145–2156 (1978)
- T.W. Lezniak, J. Winckler, Experimental study of magnetospheric motions and the acceleration of energetic electrons during substorms. *J. Geophys. Res.* **75**(34), 7075–7098 (1970)
- W. Magnes, O. Hillenmaier, U. Auster, P. Brown, S. Kraft, J. Seon, M. Delva, A. Valavanoglou, S. Leitner, D. Fischer, J. Wilfinger, C. Strauch, J. Ludwig, D. Constantinescu, K.H. Fornacon, K. Gebauer, D. Hercik, I. Richter, J. Eastwood, J.P. Luntama, G.W. Na, C.H. Lee, A. Hilgers, *Sosmag: Space Weather Magnetometer Aboard Geo-Kompsat-2a* (2019)
- A.G. Opp, Penetration of the magnetopause beyond 6.6 RE during the magnetic storm of January 13–14, 1967: introduction. *J. Geophys. Res.* **73**(17), 5697–5698 (1968)
- S. Pak, Y. Shin, J. Woo, J. Seon, A numerical method to analyze geometric factors of a space particle detector relative to omnidirectional proton and electron fluxes. *J. Korean Astron. Soc.* **5**(4), 111–117 (2018). <https://doi.org/10.5303/JKAS.2018.51.4.111>

- G.K. Parks, *Physics of Space Plasmas* (Westview Press, Boulder, 2004)
- D.M. Sawyer, J.I. Vette, Ap-8 trapped proton environment for solar maximum and solar minimum. NASA STI/Recon Technical Report N 77 (1976)
- A. Sicard-Piet, S. Bourdarie, D. Boscher, R. Friedel, M. Thomsen, T. Goka, H. Matsumoto, H. Koshiishi, A new international geostationary electron model: IGE-2006, from 1 keV to 5.2 MeV. *Space Weather* **6**(7), S07003 (2008)
- T.L. Skillman, M. Sugiura, Magnetopause crossing of the geostationary satellite ATS 5 at 6.6 RE. *J. Geophys. Res.* **76**(1), 44–50 (1971)
- J. Sullivan, Geometric factor and directional response of single and multi-element particle telescopes. *Nucl. Instrum. Methods* **95**(1), 5–11 (1971)
- A.J. Tylka, J.H. Adams, P.R. Boberg, B. Brownstein, W.F. Dietrich, E.O. Flueckiger, E.L. Petersen, M.A. Shea, D.F. Smart, E.C. Smith, Creme96: a revision of the cosmic ray effects on micro-electronics code. *IEEE Trans. Nucl. Sci.* **44**(6), 2150–2160 (1997)
- K. Yando, R.M. Millan, J.C. Green, D.S. Evans, A Monte Carlo simulation of the NOAA POES medium energy proton and electron detector instrument. *J. Geophys. Res. Space Phys.* **116**(A10), A10231 (2011)